J. Fluid Mech. (2025), *vol.* 1018, A26, doi:10.1017/jfm.2025.10511

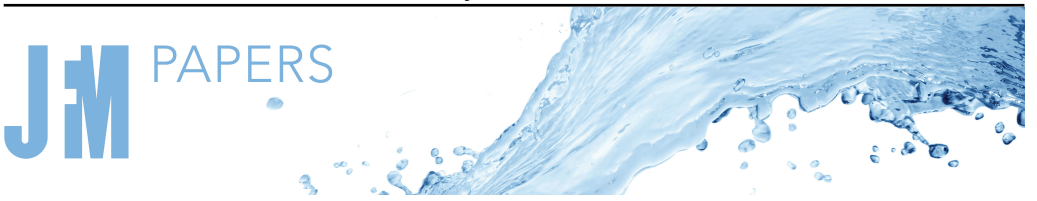

The interplay of flow-induced, gravitational and mechanical compaction in soft porous media

Emma Rose Bouckley[1], **Benjamin Sourcis**[2] **and Duncan Robin Hewitt**[1]

[1]DAMTP, Centre for Mathematical Sciences, Wilberforce Road, Cambridge CB3 0WA, UK

[2]Saint-Gobain Recherche, 41 Quai Lucien Lefranc, B.P. A35, Aubervilliers CEDEX F-93303, France

Corresponding author: Emma Rose Bouckley, eb775@cam.ac.uk

(Received 21 February 2025; revised 28 May 2025; accepted 26 July 2025)

Flow-induced compaction of soft, elastically deformable porous media occurs in numerous industrial processes. A theoretical study of this problem, and its interplay with gravitational and mechanical compaction, is presented here in a one-dimensional configuration. First, it is shown that soft media can be categorised into two 'types', based on their compaction behaviour in the limit of large applied fluid pressure drop. This behaviour is controlled by the constitutive laws for effective pressure and permeability, which encode the rheology of the solid matrix, and can be linked to the well-known poroelastic diffusivity. Next, the interaction of gravitational and flow-induced compaction is explored, with the resultant asymmetry between upward and downward flow leading to distinct compaction behaviour. In particular, flow against gravity – upwards – must first relieve gravitational stresses before any bulk compaction of the medium can occur, so upward flow may result in compaction of some regions and decompaction of others, such that the overall depth remains fixed. Finally, the impact of a fixed mechanical load on the sample is considered: again, it is shown that flow must 'undo' this external load before any bulk compaction of the whole medium can occur in either flow direction. The interplay of these different compaction mechanisms is explored, and qualitative differences in these behaviours based on the 'type' of the medium are identified.

Key words: porous media

1. Introduction

A saturated, soft porous medium consists of a deformable solid matrix and interconnected pore space filled with fluid. The study of such deformable media, which constitutes the field of poromechanics (Coussy 2004), was originally established to understand

soil mechanics (Biot 1941; Terzaghi 1943) and has expanded to include applications to biological media (Khaled & Vafai 2003; Boschetti *et al.* 2004; Fung 2013), geophysics (Hewitt, Chini & Neufeld 2018) and industrial processes (Fitt *et al.* 2002). In flow through rigid porous media, the solid matrix merely acts as a conduit through which the fluid percolates (Bear 1996). In contrast, in soft porous media, deformation of the solid structure can drive fluid motion, while fluid motion, in turn, can induce deformation of the solid matrix. If the deformation is large enough, then this interaction can lead to complex mechanics, as deformation of the solid can reduce permeability, impeding further fluid flow. In this paper, we will consider how flow-induced compaction of soft porous media interacts with gravitational and mechanical compaction.

Mechanical compaction refers to the external application of a load that deforms the solid matrix, inducing the flow of interstitial fluid. This problem has been the subject of numerous studies, mainly focused on the transient response to a fixed or varying applied load. For instance, in a biological context, the periodic loading of porous media is typical in tissues and is essential for solute transport (Fiori *et al.* 2023, 2025). Indeed, biological porous media often respond dynamically to mechanical loading, optimising resource use and resilience. For example, in bones, regular heavy loading increases bone density, while disuse leads to significant loss of bone density, which is of medical interest in long-term bed-rest patients and astronauts in microgravity (Smit 2022). Particular industrial motivation comes from the dewatering of solid–fluid mixtures (Landman, Sirakoff & White 1991; Hewitt *et al.* 2016*b*; Paterson *et al.* 2021), known as pressure filtration, which is utilised in paper production (Fitt *et al.* 2002) and waste reduction (Wakeman 2007). There are also applications to geophysical problems, such as the modelling of glaciers and pressure-driven magma eruptions (Manga & Brodsky 2006; Hewitt *et al.* 2018).

Flow-induced compaction is markedly different from mechanical compaction. When a medium is subjected to a steady external load, the solid matrix compacts uniformly as it is placed under uniform stress. In contrast, flow of interstitial fluid exerts viscous drag on the matrix and induces deformation that is characteristically non-uniform, since the gradient of fluid pressure exerts a gradient of stress. This phenomenon was elegantly illustrated in experiments by Parker, Mehta & Caro (1987), and has been the subject of various experimental and theoretical studies since then (MacMinn, Dufresne & Wettlaufer 2015; Hewitt *et al.* 2016*a*; Paterson *et al.* 2019). Some recent work has gone beyond the behaviour in the bulk medium to also explore the influence of the boundary conditions on the response of the medium to flow, particularly considering an interfacial permeability that differs from that of the bulk (Feng & Young 2020; Xu *et al.* 2022, 2024).

The force of gravity arising from the density difference between the deformable medium and interstitial fluid is often neglected in these studies, where it is assumed to be much weaker than other driving forces. There are, however, some situations where such gravitational forces play an important role, such as in the compaction of sedimentary basins (Smith 1971; Audet & Fowler 1992) and subsurface soil or ice (Head & Wilson 1992; Wilson & Head 1994; Mergny & Schmidt 2024). Gravity also drives industrial settling problems, known as gravity thickening (Buscall & White 1987; Chu & Lee 2002; Concha & Bürger 2002; Chu, Lee & Tay 2003), and is an important consideration in the field of compressive rheology (Landman & White 1994; de Kretser, Boger & Scales 2003; Stickland & Buscall 2009).

Most of these studies have examined mechanical, flow-induced or gravitational compaction in isolation, justified by relevant applications where one of these features is dominant. It is also common to assume that any deformation is small and linear, which significantly simplifies theoretical modelling (Biot 1941). Here, we will instead explore the interplay between these three distinct forms of compaction, considering that

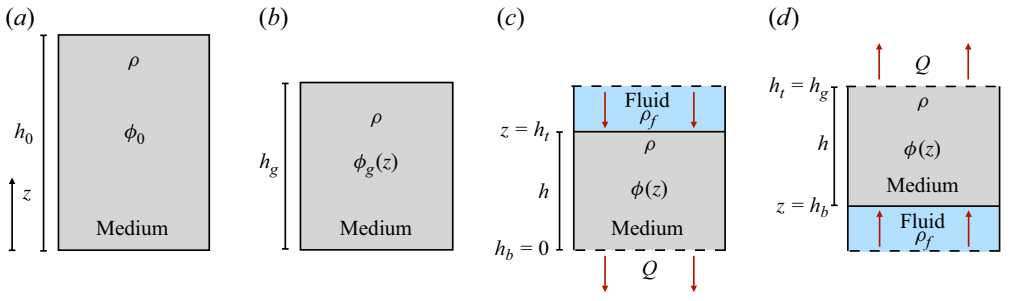

Figure 1. The set-up for §§ 2–4. (*a*,*b*) No flow ($\Delta p = 0$) with (*a*) $\Delta\rho = \rho_s - \rho_f = 0$, stress-free, and (*b*) $\Delta\rho > 0$, gravity-slumped. (*c*,*d*) The subsequent flow-induced compaction set-up, with $\Delta\rho > 0$, for flow applied (*c*) downwards ($Q < 0$, driven by a negative pressure drop $\Delta p < 0$) and (*d*) upwards ($Q > 0$, driven by a positive pressure drop $\Delta p > 0$). The upper and lower walls are permeable to the fluid, but not to the solid.

the stresses from each are of comparable size and allowing for large-scale nonlinear deformation. Such interaction is particularly common in industrial applications, where gravitational settling can interact with both external mechanical forcing and fluid flow through a soft, deformable porous medium to affect its overall compaction. This is the case in the production of metallic syntactic foam, for example, which involves molten metal flowing through a solid matrix of hollow mini-spheres (Borovinšek *et al.* 2016; de la Muela *et al.* 2020; Fiedler *et al.* 2020), or in the production of fibreglass insulation, where air flows through the soft fibrous medium (Cameron & Rapp 2001); similar interplay is also encountered in the processing of wet wood pulp (Fitt *et al.* 2002). Here, we will approach this problem from a theoretical standpoint, focusing on simple unidirectional flow either with or against the direction of gravity, and either without or with additional mechanical confinement. For the latter, we consider the steady application of a uniform displacement – or 'pre-strain' – at the boundary.

After laying out the model framework in § 2, we set the scene in § 3 by reconsidering the problem in the absence of gravity. We classify media into one of two generic 'types', based on their constitutive laws for permeability and effective pressure. Gravitational stresses are subsequently included to explore the implication of gravity with downward flows. We then explicitly consider upward flows in § 4, and quantify the implication of the asymmetry between upward and downward flows. Finally, in § 5, we introduce pre-straining into the model, such that the medium is mechanically compressed between two porous plates while flow is induced. We aim to provide a comprehensive understanding of the interaction between compaction driven by flow in soft porous media and compaction due to gravity, or simply due to the application of an external load.

2. Model set-up

2.1. *Governing equations and boundary conditions*

Consider a fully saturated porous medium, which is initially unstrained in the absence of flow and gravitational stresses. We let ϕ denote the solid fraction of the porous medium, and z denote the vertical axis; in the unstrained state, the medium has uniform stress-free solid fraction $\phi(z) = \phi_0$ and occupies depth h_0 (see figure 1*a*). The medium is composed of solid phase with density ρ_s and fluid phase with density ρ_f such that its bulk density is $\rho = \rho_s\phi + \rho_f(1-\phi)$. When $\rho_s > \rho_f$, the medium differentially compacts under gravity to depth $h_g < h_0$ with solid fraction profile $\phi_g(z)$; we refer to this state as 'gravity-slumped' (see figure 1*b*).

Consider now that the gravity-slumped medium is lying between semi-permeable plates at $z = 0$ and $z = h_g$, which allow the fluid phase to freely pass through but do not allow passage of the solid phase. When an excess fluid pressure drop Δp is applied across the sample, fluid flows through the medium with velocity $w_f(z)$, which drives deformation of the medium itself with solid velocity $w_s(z)$. We consider unidirectional flow, which may be generated in either vertical direction, depending on the sign of Δp (see figures 1*c*,*d*), and we choose to specify that a positive Δp drives upward flow in the positive z direction. As compaction occurs, the solid fraction profile $\phi(z)$ evolves, and the medium compacts to a depth $h = h_t - h_b$, where $z = h_b$, h_t are the positions of the bottom and top boundaries of the medium, respectively. The boundary out of which fluid flows remains fixed in position as the medium compacts against the relevant semi-permeable plate.

We consider both the solid and fluid phases to be individually incompressible, and enforce conservation of mass in each phase, Darcy's law and total stress balance to give

$$-\frac{\partial \phi}{\partial t} + \frac{\partial}{\partial z}[(1-\phi)w_f] = 0, \tag{2.1}$$

$$\frac{\partial \phi}{\partial t} + \frac{\partial}{\partial z}[\phi w_s] = 0, \tag{2.2}$$

$$(1-\phi)(w_f - w_s) = -\frac{k}{\mu}\left(\frac{\partial p}{\partial z} + \rho_f g\right), \tag{2.3}$$

$$\frac{\partial \Pi}{\partial z} + \rho g = 0, \tag{2.4}$$

where k is the permeability of the medium, μ is the fluid viscosity, p is the local pressure in the fluid, g is the gravitational acceleration, and Π is the total pressure of the two-phase system. In line with standard poromechanical modelling, we further define the effective pressure $\sigma = \Pi - p$ such that (2.3) and (2.4) become

$$(1-\phi)(w_f - w_s) = \frac{k}{\mu}\left(\frac{\partial \sigma}{\partial z} + \Delta\rho\, g\phi\right), \tag{2.5}$$

where $\Delta\rho = \rho_s - \rho_f$. The effective pressure σ and permeability k are material constitutive functions that encode the rheology of the medium. We refine our focus to general elastic media such that σ depends only on the vertical strain, or equivalently, on the solid fraction ϕ (MacMinn, Dufresne & Wettlaufer 2016). The stress-free solid fraction ϕ_0, introduced above, satisfies $\sigma(\phi_0) = 0$. We similarly assume that the permeability $k(\phi)$ depends only on the current solid fraction of the medium.

We must enforce that solid velocity is zero at the boundary out of which fluid flows. As such, $w_s(z = h_t) = 0$ in upward flow and $w_s(z = h_b) = 0$ in downward flow. The solid velocity at the opposite boundary is given simply by $w_s(h_{b,t}) = \partial h_{b,t}/\partial t$. At the upper boundary $z = h_t$, we scale the pore pressure p to zero, thus at the lower boundary $p(h_b) = \rho_f g h + \Delta p$, since Δp is the applied pressure drop in excess of the background hydrostatic pressure.

The asymmetry induced by gravity requires the specification of different boundary conditions for Π in upward and downward flows. We focus first on the case of downward flow ($\Delta p < 0$); the boundary conditions for upward flow need more care and are presented in § 4.

In the absence of flow, the total pressure at the upper boundary is zero, $\Pi(h_t) = 0$. The pressure at the lower boundary follows from (2.4) and consists of the relative weight per unit area of the overlying solid and fluid. We neglect any additional resistance to flow coming from the entry conditions to the porous medium (e.g. Xu *et al.* 2022) and as

such, the total pressure at the upper boundary remains zero in the presence of downward flow. These pressure boundary conditions for downward flow can be expressed in terms of effective pressure σ:

$$\sigma|_{z=h_t} = 0, \tag{2.6}$$

$$\sigma|_{z=h_b} = \Delta\rho g h_0 \phi_0 + |\Delta p|, \tag{2.7}$$

where the dependence on ϕ has been simplified by recognising that conservation of total solid mass enforces

$$\int_{h_b}^{h_t} \phi \, \mathrm{d}z = h_0 \phi_0. \tag{2.8}$$

2.2. *Non-dimensionalisation*

This system of equations is closed by the specification of constitutive laws for the permeability k and the effective pressure σ. Given such laws, we can extract characteristic dimensional scales for the elastic modulus σ^* and permeability k^*. To remove dimensions from the problem, we scale lengths with the stress-free depth h_0, pressures with σ^*, velocity with $k^*\sigma^*/h_0\mu$, and time with $h_0^2\mu/k^*\sigma^*$, the poroelastic time scale. Non-dimensionalisation introduces two dimensionless groups,

$$\mathcal{G} = \frac{\Delta\rho g h_0}{\sigma^*}, \quad \mathcal{P} = \frac{\Delta p}{\sigma^*}, \tag{2.9}$$

where $\mathcal{G}$ is a dimensionless measure of the relative importance of gravitational stress to elastic stresses, and $\mathcal{P}$ is the dimensionless pressure drop. We can also frame the relative gravity term $\mathcal{G}$ in the context of the compaction length scale $L = \sigma^*/\Delta\rho g$ (Head & Wilson 1992; Wilson & Head 1994; Mergny & Schmidt 2024), such that $\mathcal{G} = h_0/L$ is a ratio of the medium's depth to the depth over which gravitational compaction occurs; when $L \gg h_0$, little gravitational compaction is expected.

The material flux Q is defined by

$$Q \equiv \phi w_s + (1-\phi) w_f, \tag{2.10}$$

which, by combining (2.1)–(2.2), is constant in space. Equation (2.3) with all variables now dimensionless is

$$(1-\phi)(w_f - w_s) = k(\phi)\left(\sigma' \frac{\partial \phi}{\partial z} + \mathcal{G}\phi\right), \tag{2.11}$$

using the notation $\sigma' = \partial\sigma/\partial\phi$. The flux can therefore be identified as

$$Q = w_s + k(\phi)\left(\sigma' \frac{\partial \phi}{\partial z} + \mathcal{G}\phi\right), \tag{2.12}$$

and the boundary conditions (2.6)–(2.7) become

$$\sigma|_{z=h_t} = \sigma(\Phi_t) = 0, \tag{2.13}$$

$$\sigma|_{z=h_b} = \sigma(\Phi_b) = \mathcal{G}\phi_0 + |\mathcal{P}|, \tag{2.14}$$

where we have introduced notation for the solid fraction at the respective boundaries $\Phi_t = \phi(z = h_t)$ and $\Phi_b = \phi(z = h_b)$. By assuming that the constitutive law $\sigma(\phi)$ is invertible, we can simply transform (2.13)–(2.14) into conditions on $\Phi_{t,b}$. Note simply that in a downward flow, the upper boundary is stress-free and $\Phi_t = \phi_0$.

Our primary concern here is to explore the steady solutions of compaction, but a brief summary of transient solutions is presented in Appendix A, which also serves as

a numerical validation of the following steady solutions. In a steady state, it is most convenient to transform the mass conservation equation (2.8) into an integral over ϕ using (2.12) with $w_s \equiv 0$, to yield an implicit equation for the unknown flux Q:

$$\int_{\Phi_b}^{\Phi_t} \frac{k\sigma'\phi}{Q - k\mathcal{G}\phi}\,\mathrm{d}\phi = \phi_0. \tag{2.15}$$

Having determined Q, the depth h follows from direct integration of (2.12),

$$\int_{\Phi_b}^{\Phi_t} \frac{k\sigma'}{Q - k\mathcal{G}\phi}\,\mathrm{d}\phi = h, \tag{2.16}$$

while the solid fraction profile $\phi(z)$ follows implicitly from integrating only up to z,

$$\int_{\Phi_b}^{\phi} \frac{k\sigma'}{Q - k\mathcal{G}u}\,\mathrm{d}u = z(\phi) - h_b, \tag{2.17}$$

where $h_b \equiv 0$ in downward flow.

We can identify the grouping $D = k\sigma'\phi$ in (2.15) as the dimensionless form of the poroelastic diffusivity $D^* = k\sigma'\phi/\mu$, which is well known to control the essential behaviour of poroelastic compaction, and is related to the poroelastic time scale $h_0^2\mu/k^*\sigma^*$ (Landman *et al.* 1991; Audet & Fowler 1992; Worster, Peppin & Wettlaufer 2021). As we will see, the dependence on the combination $k\sigma'$, which is the product of the permeability and the effective stiffness of the medium, reflects the intrinsic interplay of these features in the mechanics of this problem, and dictates the qualitative behaviour of the deformable medium under compaction.

2.3. *Constitutive laws*

The model outlined above is defined for any constitutive laws for permeability $k(\phi)$ and any invertible effective pressure $\sigma(\phi)$ that are functions of solid fraction ϕ alone. When considering solutions to the model, we will focus our attention on specific choices for these laws. Generally, these laws must follow some physically intuitive restrictions. In particular, the medium cannot be compacted beyond a maximum solid fraction, $\phi_m \leqslant 1$; this identifies a corresponding minimum solid depth $h_m = \phi_0 h_0/\phi_m$ at which the medium is uniformly held at the maximum solid fraction. We choose the permeability to vanish at the maximum solid fraction ϕ_m but to diverge as the solid fraction tends to zero. Similarly, we require the effective pressure to vanish at the stress-free solid fraction ϕ_0, and we also expect it to diverge as $\phi \to \phi_m$. These effects are captured by simple laws of the general form

$$k = \frac{(\phi_m - \phi)^\delta}{\phi^\eta}, \quad \sigma = \frac{(\phi - \phi_0)^\gamma}{(\phi_m - \phi)^\lambda}, \tag{2.18}$$

for δ, η, γ, $\lambda > 0$.

For the purposes of illustrating model results, we set $\delta = 3$, $\eta = 2$, $\gamma = 1$, and leave λ as a free parameter. The choices of δ and η are motivated by the widely used Kozeny–Carman permeability law for the modelling of uniform packed spheres (Carman 1997), while the choice of γ is made to specify a linear relation between σ and ϕ for small deformations. As such, all solutions presented here are governed by the laws

$$k = \frac{(\phi_m - \phi)^3}{\phi^2}, \quad \sigma = \frac{(\phi - \phi_0)}{(\phi_m - \phi)^\lambda}, \tag{2.19}$$

where results will be sensitive to choice of λ. For simplicity, for the rest of this paper we will set $\phi_m = 1$ and $\phi_0 = 0.6$.

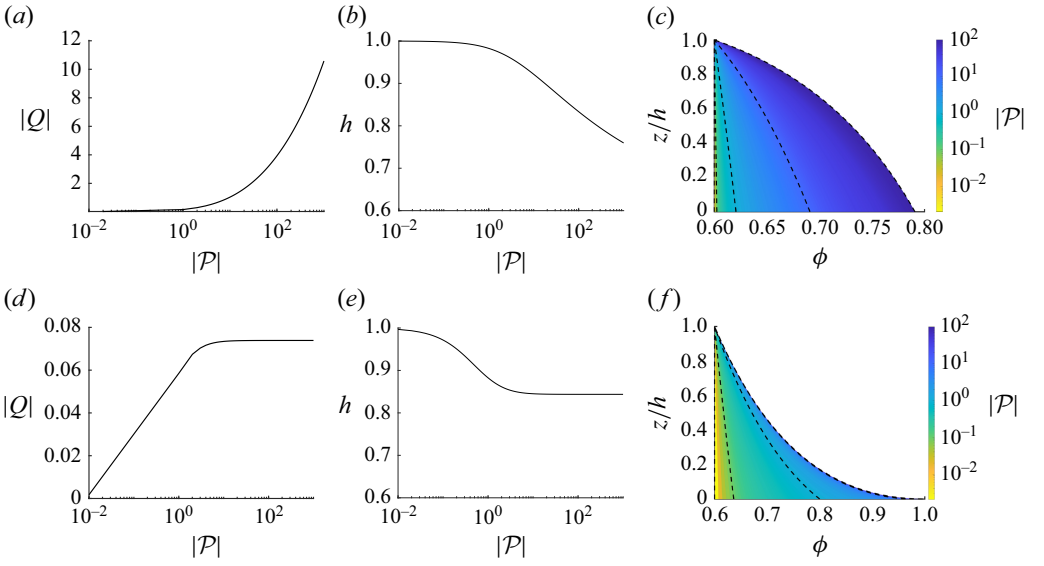

Figure 2. Steady-state solutions for a medium compacted by a downward flow induced by pressure drop $\mathcal{P} < 0$, showing (*a*,*d*) the flux Q and (*b*,*e*) the depth h as functions of pressure drop. (*c*,*f*) Graphs of the scaled solid fraction profiles $\phi(z/h)$. Solutions are presented for media governed by two different effective pressure laws given by (2.19), with (*a–c*) $\lambda = 4$ and (*d–f*) $\lambda = 1$.

Note that in the chosen flow set-up (figure 1), the system can never be in a state of negative effective pressure (i.e. $\phi < \phi_0$). In such a state, the constitutive behaviour would vary significantly depending on whether the medium was cohesive (like a sponge) or comprised a collection of deformable particles (like a pack of hydrogel beads). For example, flow upwards through a collection of particles without confinement can lead to fluidisation (Van Zessen *et al.* 2005), which is not considered here.

3. Solutions and analysis of model

3.1. *Observations when* $\mathcal{G} = 0$

We first consider solutions when $\mathcal{G} = 0$, as would be the case if, for example, the porous medium comprised solid and fluid phases with comparable densities. While this case has been the focus of previous work (Parker *et al.* 1987; Paterson *et al.* 2019), it will be helpful to interrogate this limit a little further here to set the scene for the remainder of this work. In this situation, upward and downward flows are identical. Figure 2 illustrates flux Q, depth h, and profiles of solid fraction ϕ as a downward flow is induced with increasing pressure drop $|\mathcal{P}|$ across the medium. Flow through the porous medium induces differential compaction that results in denser packing at the lower boundary, where the fluid exits, while the medium remains stress-free at the upper boundary, where fluid enters.

Figure 2 highlights two possible behaviours for compaction as $|\mathcal{P}|$ increases for two media with different constitutive laws. The first medium (figure 2*a–c*) shows a continual increase in Q with $\mathcal{P}$; this is the standard behaviour for a rigid porous medium, but extends to deformable media if they remain sufficiently permeable under increasing compaction. The depth h decreases towards the minimum solid depth $h_m = 0.6$, and ϕ correspondingly compacts towards the maximum solid fraction $\phi_m = 1$, although this limit is not attained at finite $\mathcal{P}$. The second medium (figure 2*d–f*) illustrates the existence of a maximal value

of Q as $|\mathcal{P}|$ increases. As Q approaches this maximum, h approaches a minimum that is larger than h_m, and ϕ tends towards an asymptotic profile with a curvature different to that of the profiles in figure 2(*c*). All of these measures (Q, h, ϕ) effectively attain their asymptotic value or profile for $\mathcal{P} \approx O(1)$, and become insensitive to $\mathcal{P}$ for larger pressure drops, in clear contrast to the results in figure 2(*a*)–2(*c*). The difference between the media in this figure is that the second medium has a stiffness with a weaker dependence on ϕ than the first; that is, it stiffens less significantly under compaction. Due to its lower stiffness, the permeability – or more specifically, the loss of permeability – plays a more dominant role in determining the response of the medium: further compaction or increase in Q is more strongly opposed by the resistance to flow.

As already noted, there is a marked difference in the curvature of the compacted profiles $\phi(z)$ between the two media as the pressure drop increases. This difference is encapsulated in the contrasting gradients of solid fraction $\partial\phi/\partial z$ at the lower boundary. The profiles in figure 2(*c*) show $\partial\phi/\partial z$ tending towards zero at the lower boundary, while the solid fraction steadily compacts across the depth of the medium as $\mathcal{P}$ increases. In contrast, figure 2(*f*) illustrates a limit towards an infinite gradient at the lower boundary as the solid fraction quickly reduces away from the lower boundary value.

In the next subsection, we will classify how these observed behaviours can be predicted from the constitutive laws. Some of these ideas were briefly discussed in the appendix of Hewitt *et al.* (2016*a*), and we expand on and formalise those ideas here.

3.2. *'Types' of behaviour*

3.2.1. *Limiting flux*

In a steady state and for $\mathcal{G} = 0$, the flux is given explicitly from (2.15) by

$$Q = \frac{1}{\phi_0}\int_{\Phi_b}^{\Phi_t} k\sigma'\phi \,\mathrm{d}\phi = \frac{1}{\phi_0}\int_{\Phi_b}^{\Phi_t} D \,\mathrm{d}\phi. \tag{3.1}$$

We consider a downward flow in which a negative pressure drop $\mathcal{P}$ induces negative flux Q and has boundary conditions $\Phi_b = \sigma^{-1}(|\mathcal{P}|)$ and $\Phi_t = \phi_0$. The derivative of $|Q|$ with respect to $|\mathcal{P}|$ immediately shows

$$\frac{\partial|Q|}{\partial|\mathcal{P}|} = \frac{k\sigma'\phi}{\phi_0}\bigg|_{\Phi_b}\frac{\partial\Phi_b}{\partial\mathcal{P}} = \frac{k\phi}{\phi_0}\bigg|_{\Phi_b} > 0, \tag{3.2}$$

since $\partial\Phi_b/\partial|\mathcal{P}| = \sigma'(\Phi_b)^{-1}$. As such, the magnitude of flux must increase with increasing pressure drop across the medium. This confirms that either $|Q|$ increases without bound, or $|Q|$ increases to an asymptotic limit as $|\mathcal{P}|$ increases; the two behaviours of flux observed in figure 2 are the only two possibilities.

In order to deduce for which laws we expect flux to be unbounded or limited with increasing $|\mathcal{P}|$, we consider the limit $|\mathcal{P}| \to \infty$, following Hewitt *et al.* (2016*a*). In this limit, we expect $\phi \to \phi_m$ at the base, so we can generically express permeability and effective pressure as power laws of the form

$$k \approx (\phi_m - \phi)^{\alpha}, \quad \sigma \approx (\phi_m - \phi)^{-\beta}, \tag{3.3}$$

for some $\alpha, \beta \geqslant 0$. Note that in our chosen constitutive laws, given by (2.19), $\alpha = 3$ and $\beta = \lambda$. Considering the effective pressure at the compacted boundary $\sigma(\Phi_b) = |\mathcal{P}|$, we identify $(\phi_m - \Phi_b) \approx |\mathcal{P}|^{-1/\beta}$, therefore it follows from integration of (3.2) that the flux

scales like

$$|Q| \approx |\mathcal{P}|^{|1-\alpha/\beta|} \quad \text{for } \alpha < \beta, \tag{3.4}$$

$$|Q| \approx \ln(|\mathcal{P}|) \quad \text{for } \alpha = \beta, \tag{3.5}$$

$$|Q| \approx Q_\infty + |\mathcal{P}|^{-|1-\alpha/\beta|} \quad \text{for } \alpha > \beta, \tag{3.6}$$

as $|\mathcal{P}| \to \infty$, where Q_∞ is a constant. Two types of behaviour can be identified: type 1 ($\alpha \leqslant \beta$), for which Q is unbounded with increasing $|\mathcal{P}|$; and type 2 ($\alpha > \beta$), for which Q is bounded. This classification can be recast in terms of the diffusivity $D = k\sigma'\phi$, with type 1 corresponding to D diverging faster than a simple pole, $(\phi_m - \phi)D \to \infty$ as $\phi \to \phi_m$.

In summary, for type 1 media, k approaches zero more slowly than σ diverges as $|\mathcal{P}|$ is increased. Physically, this means that as a type 1 medium is steadily compacted towards the maximum solid fraction ϕ_m everywhere, the medium maintains sufficient permeability for flow. Therefore, like a rigid porous medium, the flux can be increased without bound simply by increasing the pressure drop. The insensitivity to loss in permeability allows for further continual compaction towards ϕ_m. For type 2 media, in contrast, k tends to zero quicker than σ diverges as $|\mathcal{P}|$ is increased, and consequently the mechanics of compaction close to the maximum solid fraction are controlled primarily by the loss of permeability. Microstructural effects enforce that at solid fractions less than the theoretical maximum ϕ_m, the medium becomes increasingly impermeable, continually impeding flow such that the magnitude of flux $|Q|$ increases asymptotically towards a finite limiting value Q_∞. Since further compaction is limited by the decreased permeability, the depth tends towards a finite compaction depth h_∞ that is larger than the theoretical minimum solid depth h_m.

In general, it is difficult to predict the 'type' of a given deformable medium due to the intrinsic dependence on the combination of permeability and stiffness. However, it is possible to find examples of constitutive laws corresponding to both 'types' in previous literature. For example, constitutive laws giving type 1 media have been reported for nylon fibres in glycerine (Hewitt *et al.* 2016*b*) and intervertebral discs (Riches *et al.* 2002). Reported type 2 media include hydrogel beads (MacMinn *et al.* 2015), cellulose fibres (Hewitt *et al.* 2016*b*), compacting shale layers (Audet & Fowler 1992) and waste water treatment sludge (Stickland & Buscall 2009).

3.2.2. *Limiting compaction profiles*

In a downward flow, the gradient of solid fraction $\partial\phi/\partial z$ at the lower compacted boundary is found from rearrangement of (2.12) and is indicative of the overall steady compaction profile $\phi(z)$. With $\mathcal{G} = 0$, the gradient in the limit $\phi \to \phi_m$ is simply $\partial\phi/\partial z \to Q(\phi_m - \phi)^{1+\beta-\alpha}$, which is dependent on the powers α, β and the limiting form of Q as defined in (3.4)–(3.6). As before, we can express $\mathcal{P}$ in terms of the compacted boundary solid fraction Φ_b through the effective pressure boundary condition; $(\phi_m - \Phi_b) \approx |\mathcal{P}|^{-1/\beta}$.

For type 1 media ($\alpha \leqslant \beta$), Q is unbounded for increasing $|\mathcal{P}|$, with precise form given by (3.4)–(3.5). Combined with the limiting expression for $|\mathcal{P}|$, we deduce that at the lower boundary, $\partial\phi/\partial z \to 0$ as $|\mathcal{P}| \to \infty$.

For type 2 media ($\alpha > \beta$), Q tends to a limiting value Q_∞, so the limit of the gradient is determined explicitly by the sign of $1 + \beta - \alpha$, giving the follow options for the gradient at the lower boundary:

(i) type 2*i* ($\beta < \alpha < \beta + 1$), $D \to \infty$, $\partial\phi/\partial z \to 0$
(ii) type 2*ii* ($\alpha = \beta + 1$), $D \to D_\infty$ (constant), $\partial\phi/\partial z \approx$ constant
(iii) type 2*iii* ($\alpha > \beta + 1$), $D \to 0$, $\partial\phi/\partial z \to \infty$.

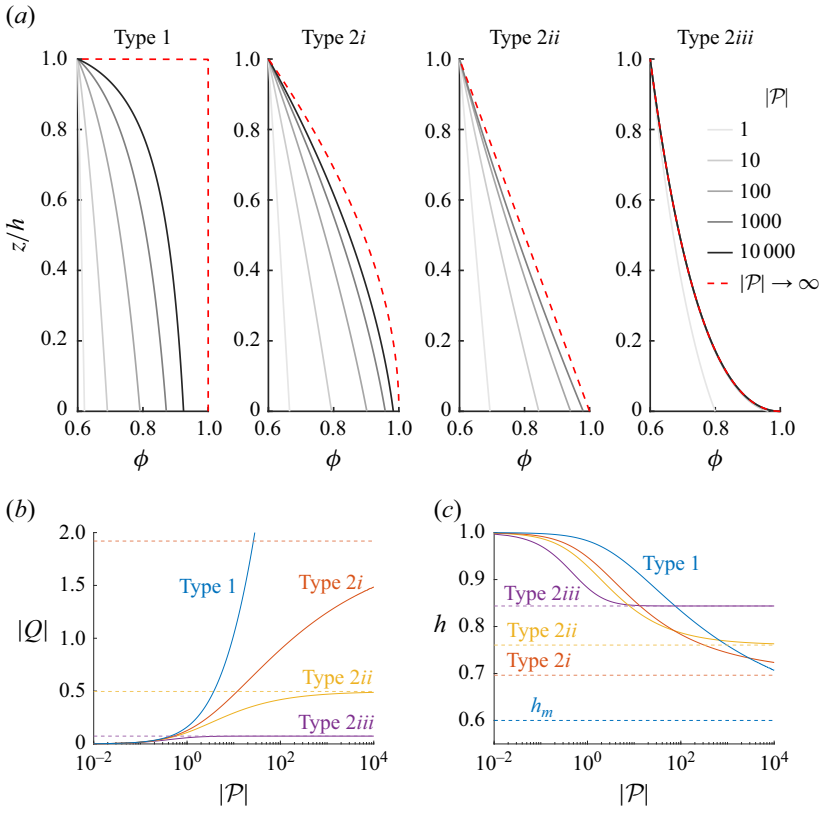

Figure 3. (*a*) Steady-state profiles for the solid fraction ϕ for different pressure drops $\mathcal{P}$ given in the legend (black lines). All solutions have $\mathcal{G} = 0$. Constitutive laws are given by (2.19) such that for type 1, $\lambda = 4$, for type 2*i*, $\lambda = 5/2$, for type 2*ii*, $\lambda = 2$, and for type 2*iii*, $\lambda = 1$. The large $\mathcal{P}$ limit for each set of laws is illustrated with red dashed lines. (*b*) The flux $|Q|$ for each type of medium plotted against applied pressure drop $\mathcal{P}$, with the limiting flux Q_∞ shown by dashed lines for each type 2 medium. (*c*) The depth h for each type, with the limiting compaction depth h_∞ and minimum depth h_m shown by dashed lines.

Figure 3 presents solutions for the solid fraction profile ϕ, flux Q and depth h as $|\mathcal{P}|$ increases, for each type of medium identified above. Type 1 media are shown to characteristically compact towards ϕ_m everywhere, with $\partial\phi/\partial z \to 0$ at the lower boundary where the fluid leaves the domain. Type 2*i* media have the same zero gradient of ϕ at the base, but they instead approach a non-uniform asymptotic $\phi(z)$ profile. Similarly, type 2*ii* and type 2*iii* media approach non-uniform asymptotic $\phi(z)$ profiles, but are differentiated by the finite gradient of ϕ at the base in type 2*ii* media, and an infinite gradient of ϕ at the base in type 2*iii*. Figures 3(*b*) and 3(*c*) illustrate the existence of limiting flux Q_∞ and limiting depth h_∞ in type 2 media. While the depth of type 1 media is of course also limited by the minimum solid depth $h_m = \phi_0/\phi_m$, in type 2 media the limiting depth h_∞ is distinct and larger than this value. We note that the order of $|\mathcal{P}|$ at which Q and h approach these limiting values increases significantly as the relative power of k to σ is decreased in the constitutive laws.

Note that these observations can be linked to the analysis of Hewitt *et al.* (2016*b*) for the formation of boundary layers under a quick moving piston for the dewatering of soft porous media. They found that in the limit $\phi \to \phi_m$, the boundary layer solutions are determined by whether D remains finite or diverges. The boundary condition for solid fraction at the

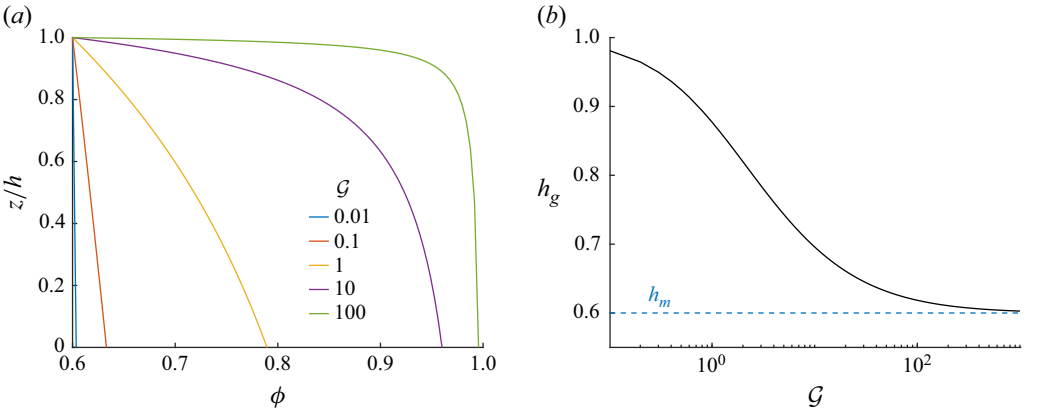

Figure 4. The gravity-slumped solutions for (*a*) profiles of solid fraction ϕ_g for different relative gravity $\mathcal{G}$ as given in the legend, and (*b*) depths h_g against increasing $\mathcal{G}$. The blue dashed line in (*b*) represents the minimum depth h_m. The medium is governed by (2.19) with $\lambda = 1$, although the illustrated behaviour is independent of medium 'type'.

medium-piston interface was found as an output of the model with finite D (type 2*ii* and 2*iii* media) corresponding to the solid fraction at this boundary attaining its maximum value and the pressure on the piston diverging, whereas $D \to \infty$ (type 1 and 2*i* media) corresponds to solid fraction approaching but not reaching the maximum.

3.3. *Gravity and type interaction*

In the absence of flow and with $\mathcal{G} > 0$, the medium non-uniformly compacts due to gravitational stresses, with denser packing at the lower boundary, and stress-free solid fraction at the upper boundary. Compaction due to gravitational stresses alone, which we call gravity-slumping, is unaffected by the permeability, unlike flow-induced compaction, so inevitably, the gravity-slumped profiles of solid fraction are different to those for flow-induced compaction (figure 4*a*). Figure 4(*b*) shows the no-flow gravity-slumped depth h_g for an example medium for increasing $\mathcal{G}$, illustrating how the medium can slump under gravity all the way down to the minimum depth h_m for sufficiently large $\mathcal{G}$. This behaviour is independent of the 'type' of the medium.

Natural and industrial porous media give rise to a wide range of relative gravity values. Even supposedly stiff porous media can have large $\mathcal{G}$ values if the relevant length scale h_0 is large enough. For example, the gravitational compaction of ice over several hundreds of metres results in $\mathcal{G} = O(10)$ (Mergny & Schmidt 2024); notably softer porous media, such as fibreglass insulation or wool stuffing, may have similar or larger relative gravity $\mathcal{G}$ on much shorter length scales ($h_0 \approx 1$ m). It is clear from figure 4(*b*) that such values of $\mathcal{G}$ can result in significant gravity-slumping, although the precise depth is highly dependent on the constitutive laws for the media.

The extension of the analysis in § 3.2 to the regime $\mathcal{G} > 0$ is more mathematically involved but draws the same conclusion of classification of types, as outlined in Appendix B. The plots in figure 5 illustrate how the interaction between gravitational and flow-induced compaction varies for type 1 and type 2 media. Under a downward flow, type 1 media can compact everywhere towards the maximum solid fraction ϕ_m as $|\mathcal{P}| \to \infty$. As such, it is unsurprising that for large enough $\mathcal{P}$, the value of $\mathcal{G}$ has a negligible impact on the profiles of ϕ (figure 5*a*). In contrast, the limiting profiles of ϕ for type 2 media in a downward flow depend sensitively on the value of $\mathcal{G}$ (figure 5*b*). Indeed, for large enough

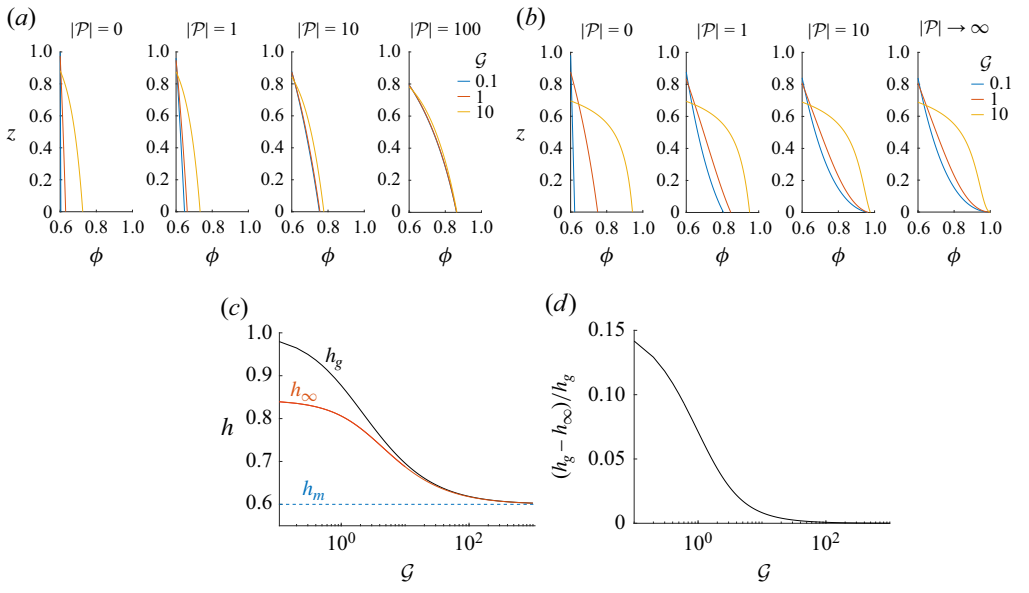

Figure 5. Steady-state solid fraction ϕ for porous media governed by constitutive laws (2.19) with (*a*) $\lambda = 4$, a type 1 medium, and (*b*) $\lambda = 1$, a type 2 medium. Solutions are shown for different pressure drops $\mathcal{P}$ inducing downward flow and different relative gravity $\mathcal{G}$, as marked. (*c*) Plots of both gravity-slumped depth h_g (black) and minimum flow-induced compaction depth h_∞ (orange) against relative gravity $\mathcal{G}$ for the type 2 medium in (*b*). The dashed blue line marks the minimum depth h_m. (*d*) Plots of the same data as in (*c*), but as relative strain $(h_g - h_\infty)/h_g$.

$\mathcal{G}$, there is little difference between the gravity-slumped profile for $\mathcal{P} = 0$ (left-hand plot) and the asymptotic profile as $|\mathcal{P}| \to \infty$ (right-hand plot); we deduce here that gravity plays the dominant role in compaction, and little further deformation by fluid flow is possible.

We can further interrogate type 2 media's dependency on $\mathcal{G}$ by observing the minimum flow-induced compaction depth h_∞ for increasing $\mathcal{G}$. Figure 5(*c*) overlays h_∞ onto the results of figure 4(*b*); increasing $\mathcal{G}$ decreases both the initial flow-free depth h_g and the limiting depth h_∞. However, if we instead inspect the relative change in depth $(h_g - h_\infty)/h_g$ in figure 5(*d*), which can be considered as the actual flow-induced strain, then we observe that this induced strain is decreasing as $\mathcal{G}$ increases. This is not surprising: since the initial gravity-slumped state is compacting towards the maximum solid fraction ϕ_m, the medium is under higher initial pressure and is therefore harder to further compact by flow. As such, we can conclude that increasing relative gravity results in less flow-induced strain in type 2 media, despite the fact that lower depths are reached.

4. Upward flow

We now extend our work to allow for an upward flow by reconsidering the effective pressure boundary conditions (2.13)–(2.14). A gravity-slumped medium takes up a non-uniform gravitational pressure that consists of the relative weight per unit area of the overlying fluid and solid. The medium compacts to a depth h_g with solid fraction profile $\phi_g(z)$ (figure 6*a*). We have previously considered downward flow, in which the fluid enters through the stress-free upper boundary, and drives further compaction. In contrast, in upward flow, the fluid enters through the gravitationally stressed lower boundary, and will drive compaction near the upper boundary. In this case, we expect that the stressed

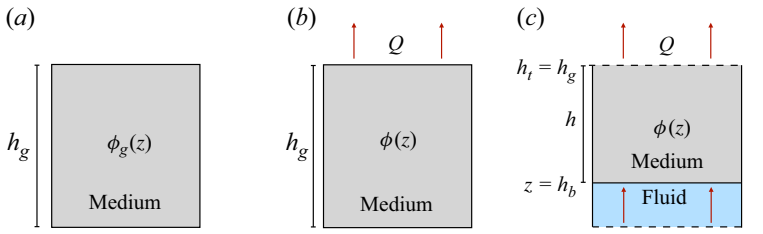

Figure 6. The set-up for § 4: (*a*) gravity-slumped ($G > 0$ and no flow $\mathcal{P} = 0$); and (*b,c*) an upward flow ($Q > 0$) driven by a positive pressure drop ($\mathcal{P} > 0$). In (*b*), the flow is slow enough such that the entry boundary pressure is not relieved ($\sigma(\Phi_e) > 0$) and the depth is fixed at h_g. In (*c*), $\mathcal{P}$ is large enough that the entry boundary pressure is relieved ($\sigma(\Phi_e) = 0$) and the depth h reduces.

lower region will decompact in response to the compaction in the upper region, and the medium may maintain a fixed depth as internal rearrangement occurs ($h = h_g$; figure 6*b*). Eventually, strong enough flow will be able to 'remove' all the gravitational pressure, leaving the lower boundary stress-free, and allowing the depth of the medium to evolve ($h < h_g$; figure 6*c*).

4.1. *Inclusion in the model*

We previously established that for downward flow, the total pressure Π and fluid pressure p disappear at the upper boundary, which is therefore stress-free. Upward flow, however, enters through the stressed lower boundary, so the equivalent boundary conditions are not so straightforward. As discussed above, flow reduces the entry boundary pressure by an amount that is *a priori* unknown, since it relies on how the medium rearranges internally. Given (2.4), we can determine the effective pressure boundary conditions up to a constant Σ:

$$\sigma(\Phi_t) = \mathcal{P} - \Sigma(\mathcal{P}), \tag{4.1}$$

$$\sigma(\Phi_b) = \mathcal{G}\phi_0 - \Sigma(\mathcal{P}), \tag{4.2}$$

where the relieved pressure Σ evolves with applied pressure drop $\mathcal{P}$ and is bounded by $0 \leqslant \Sigma \leqslant \mathcal{G}\phi_0$, enforcing $\sigma > 0$ everywhere. Note here that the pressure felt at the upper boundary due to $\mathcal{P}$ is equally reduced as pressure is taken up by the internal rearrangement of the solid fraction as gravitational compaction is 'undone'.

While the entry pressure has not been fully relieved ($\sigma(\Phi_b) > 0$), the medium is able to simultaneously compact and decompact, maintaining a fixed depth h_g. Once $\sigma(\Phi_b) = 0$, or equivalently $\Sigma = \mathcal{G}\phi_0$, the medium can no longer decompact, and further increase in $\mathcal{P}$ will drive bulk compaction ($h < h_g$). Having non-dimensionalised as in § 2.2, this mechanism is included in the steady equations (2.15)–(2.16) with the adapted boundary conditions (4.1)–(4.2), as follows:

$$\int_{\Phi_b}^{\Phi_t} \frac{k\sigma'\phi}{Q - k\mathcal{G}\phi}\,\mathrm{d}\phi = \phi_0, \tag{4.3}$$

$$\int_{\Phi_b}^{\Phi_t} \frac{k\sigma'}{Q - k\mathcal{G}\phi}\,\mathrm{d}\phi = \begin{cases} h_g & \text{for } \sigma(\Phi_b) > 0, \\ h & \text{for } \sigma(\Phi_b) = 0. \end{cases} \tag{4.4}$$

If $\sigma(\Phi_b) > 0$, then the unknowns in (4.3)–(4.4) are Σ and Q, with $h = h_g$ known. If, instead, $\sigma(\Phi_b) = 0$, then the two unknowns are h and Q. We denote the value of $\mathcal{P}$ that separates these two cases to be the 'lift-off' pressure $\mathcal{P}_{lift}$, found by setting both $h = h_g$ and $\sigma(\Phi_b) = 0$ in (4.3)–(4.4).

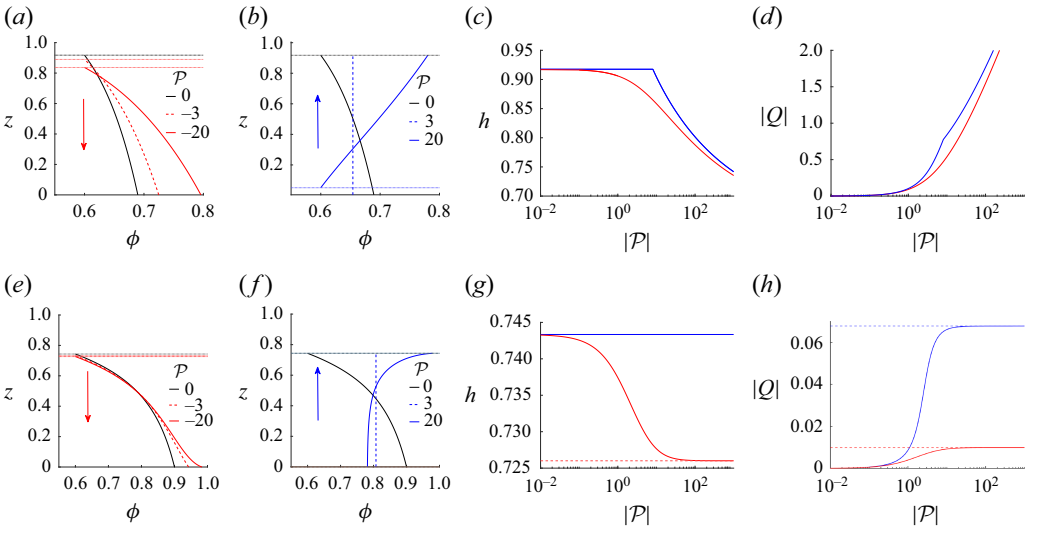

Figure 7. Steady solutions for initially gravity-slumped media (black) with $\mathcal{G} = 5$ governed by constitutive laws (2.19), with (*a–d*) $\lambda = 3$, type 1 medium, and (*e–h*) $\lambda = 1$, type 2 medium. (*a*,*b*,*e*,*f*) Solid fraction profiles ϕ for media compacted by (*a*,*e*) a downward flow (red), and (*b*,*f*) an upward flow (blue). The corresponding depth h and flux $|Q|$ evolutions are in (*c*,*g*) and (*d*,*h*), respectively.

4.2. *General solutions*

Gravity immediately introduces an asymmetry between upward and downward flow. We present in figure 7 a simple comparison of this asymmetry in both type 1 and type 2 example media. Figures 7(*a*) and 7(*b*) compare the profiles of solid fraction under compaction by downward and upward flow, respectively, in a type 1 medium, highlighting three key features. First, upward flow acts to 'undo' compaction due to gravity: inducing a downward flow can only compact the medium more, whereas upward flow allows for some initial decompaction of the medium. Second, in upward flow, there is a range of low pressure drop in which the depth remains fixed at depth h_g. Finally, during this fixed depth regime, flow-induced compaction can rearrange the internal packing of the medium to a uniform profile of solid fraction when the applied pressure drop $\mathcal{P}$ exactly balances the gravitational pressure $\mathcal{G}\phi_0$ on the lower boundary. This homogenisation of the medium must occur in the regime of fixed depth, as it requires both boundaries to be somewhat compacted. Figures 7(*e*) and 7(*f*) illustrate the same ideas in a type 2 medium.

In considering the evolution of depth h and flux Q (figure 7*c*,*g*,*d*,*h*), we note that upward flow consistently corresponds to a larger depth (less compacted) and higher flux compared to downward flow. Upward flow must first 'undo' gravitational compaction, and as such, the pressure is taken up by the rearrangement of internal packing, resulting in a reduced effective pressure at the boundary out of which flow exits. For any given pressure drop $\mathcal{P}$, we can expect downward flow to result in greater compaction and more dense packing, thus lowering the bulk permeability. We consider that the resistivity of the medium to flow is higher in a downward flow, and as such, flux is impeded. Consequently, the limiting depths h_∞ and flux $|Q_\infty|$ in type 2 media will always be lower for a downward flow.

Figure 8 presents the lift-off pressure $\mathcal{P}_{lift}$ for changing relative gravity $\mathcal{G}$ in both type 1 and type 2 media. Increasing $\mathcal{G}$ will increase gravitational compaction, so must increase $\mathcal{P}_{lift}$. While this increase is continual in the type 1 medium, in a type 2 medium it becomes unbounded at a finite value of $\mathcal{G}$ (figure 8*b*). Beyond this critical $\mathcal{G}$, no such $\mathcal{P}_{lift}$ exists:

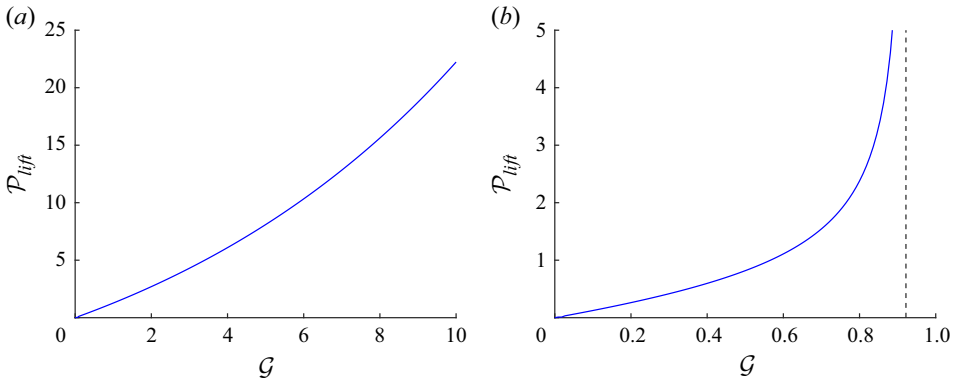

Figure 8. Lift-off pressure $\mathcal{P}_{lift}$ against relative gravity $\mathcal{G}$ for media governed by constitutive laws (2.19) with (*a*) $\lambda = 3$, a type 1 medium, and (*b*) $\lambda = 1$, a type 2 medium. The dashed line in (*b*) illustrates the asymptote of $\mathcal{P}_{lift}$.

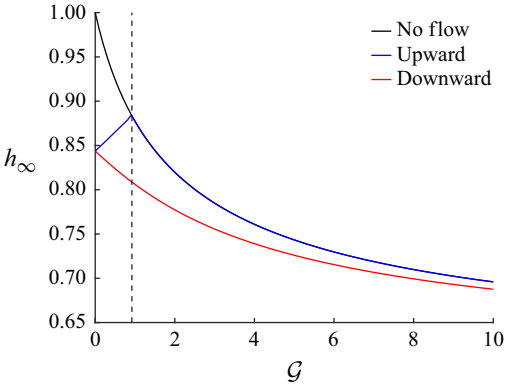

Figure 9. The limiting compaction depth h_∞ against relative gravity $\mathcal{G}$ for a type 2 medium governed by (2.19) with $\lambda = 1$. Solutions are presented for upward (blue) and downward (red) flow, together with the no-flow gravity-slumped depth h_g (black). The dashed line shows the critical $\mathcal{G}$ above which the lift-off pressure for upward flow is unbounded.

no pressure drop is able to induce bulk compaction in an upward flow, and the depth remains fixed at h_g. The example illustrated in figure 7(*g*) falls in this range, and h will remain fixed for any $\mathcal{P}$.

The interaction of type 2 media with gravity is further illustrated in figure 9, which shows the limiting compaction depth h_∞ for upward and downward flow. We have already observed that increasing $\mathcal{G}$ lowers h_∞ for downward flow (figure 5*c*); here, we see the opposite trend for upward flow for $\mathcal{G}$ sufficiently small as h_∞ directly increases with $\mathcal{G}$. However, when the critical $\mathcal{G}$ at which $\mathcal{P}_{lift} \to \infty$ is exceeded, h_∞ becomes fixed at the gravity-slumped depth h_g and thus decreases with further increase in $\mathcal{G}$. In this range, flow-induced bulk compaction is no longer possible in upward flow, and the depth is controlled solely by gravity-slumping.

5. Pre-strain

Suppose now that the porous plates that contain the medium are brought closer together by the application of an external load $\mathcal{S}_0$, so that they are separated by a distance $h_i < h_g$ (figure 10*b*). The medium is compressed between the plates and takes up the

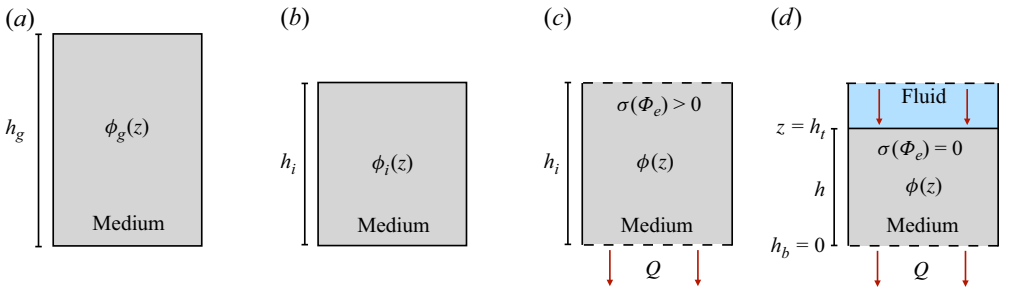

Figure 10. The set-up for § 5, showing (*a*) an unpre-strained medium with depth h_g, (*b*) the medium pre-strained to depth $h_i < h_g$, and (*c*,*d*) the pre-strained medium under different downward flows ($Q < 0$) driven by a negative pressure drop ($\mathcal{P} < 0$). In (*c*), $|\mathcal{P}|$ is small enough that the entry boundary pressure is not relieved ($\sigma(\Phi_e) > 0$) and the depth is fixed at h_i. In (*d*), $|\mathcal{P}|$ is large enough that the entry boundary pressure is relieved ($\sigma(\Phi_e) = 0$) and the depth h reduces.

uniform external load. We refer to the medium in this configuration as 'pre-strained'. If a flow is now induced across the medium by applying an excess fluid pressure drop, either upwards or downwards, then we expect the viscous flow to rearrange the solid fraction profile, compacting some regions and decompacting others. As such, if the flow is weak enough, then it should be possible for the overall depth to remain fixed at h_i (figure 10*c*), which was only possible for upward flow in the unpre-strained regime. Alternatively, for stronger flow when the entry boundary pressure is relieved, we expect that bulk compaction can still occur such that the depth evolves and the medium compacts (figure 10*d*).

5.1. *Inclusion in the model*

As with upward flow in § 4, when the entry boundary is stressed, the internal packing of the solid fraction can be rearranged, leaving the overall depth fixed at h_i (figure 10*c*). We denote this entry boundary pressure as $\sigma(\Phi_e)$, where $e = t, b$ in downward and upward flow, respectively. Once the entry pressure is relieved ($\sigma(\Phi_e) = 0$), bulk compaction occurs as $\mathcal{P}$ is increased further, such that the depth of the medium decreases ($h \leq h_i$; figure 10*d*).

We will again focus on the steady-state solutions; pre-strain is incorporated into the steady equations (2.15)–(2.16), having appropriately non-dimensionalised as in § 2.2, as follows:

$$\int_{\Phi_b}^{\Phi_t} \frac{k\sigma'\phi}{Q - k\mathcal{G}\phi}\,\mathrm{d}\phi = \phi_0, \tag{5.1}$$

$$\int_{\Phi_b}^{\Phi_t} \frac{k\sigma'}{Q - k\mathcal{G}\phi}\,\mathrm{d}\phi = \begin{cases} h_i & \text{for } \sigma(\Phi_e) > 0, \\ h & \text{for } \sigma(\Phi_e) = 0, \end{cases} \tag{5.2}$$

where $e = b$ or t. The boundary conditions are adapted from (2.13)–(2.14), but now incorporate the pre-strain pressure:

$$\sigma(\Phi_t) = \begin{cases} \mathcal{P} + \mathcal{S}_0 - \Sigma & \text{for } \mathcal{P} \geqslant 0, \\ \mathcal{S}_0 - \Sigma & \text{for } \mathcal{P} \leqslant 0, \end{cases} \tag{5.3}$$

$$\sigma(\Phi_b) = \begin{cases} \mathcal{G}\phi_0 + \mathcal{S}_0 - \Sigma & \text{for } \mathcal{P} \geqslant 0, \\ |\mathcal{P}| + \mathcal{G}\phi_0 + \mathcal{S}_0 - \Sigma & \text{for } \mathcal{P} \leqslant 0, \end{cases} \tag{5.4}$$

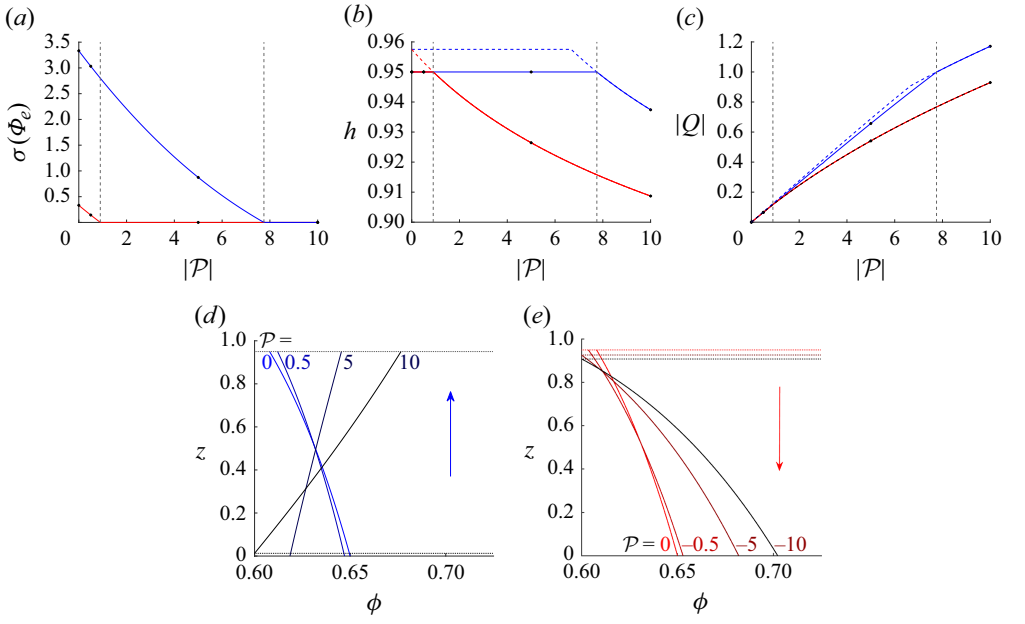

Figure 11. Steady solutions for (*a*) entry boundary pressure $\sigma(\Phi_e)$, (*b*) depth h, and (*c*) flux $|Q|$, against applied pressure drop $|\mathcal{P}|$ for a medium with $\mathcal{G}=5$, pre-strained to depth $h_i=0.95$, such that the pre-strain coefficient is $\Delta=0.008$, for upward (blue) or downward (red) flow. The profiles of solid fraction ϕ are presented in (*d*) and (*e*) for upward and downward flow, respectively, at given values of $\mathcal{P}$ denoted by dots in (*a–c*). Dashed grey lines in (*a–c*) illustrate the respective lift-off pressures $|\mathcal{P}_{lift}|$, and dashed coloured lines in (*b*,*c*) illustrate the unpre-strained solutions for depth, which coincide with the pre-strained solutions once $\sigma(\Phi_e)=0$. Dotted lines in (*d*) and (*e*) illustrate the boundaries of the medium h_b and h_t. The medium is governed by constitutive laws (2.19) with $\lambda=4$.

where $\Sigma(\mathcal{P})$ is the relieved pressure. Note that for upward flow, both the pre-strain pressure and gravitational pressure must be relieved in order to induce bulk compaction ($\Sigma=\mathcal{G}\phi_0+\mathcal{S}_0$), while downward flow need only relieve the pre-strain pressure ($\Sigma=\mathcal{S}_0$). If $\sigma(\Phi_e)>0$, then the two unknown variables in (5.1)–(5.2) are Q and Σ, with $h=h_i$ known. Alternatively, if $\sigma(\Phi_e)=0$, then the two unknowns are Q and h, and the system coincides with the compaction of an unpre-strained medium. We again denote the applied excess pressure at which the entry pressure is fully relieved to be the lift-off pressure $\mathcal{P}_{lift}$, which is found by solving (5.1)–(5.2) with $\sigma(\Phi_e)=0$ and $h=h_i$.

The initial pre-strain depth h_i and the corresponding initial pre-strain pressure $\mathcal{S}_0$ are related by the solution of (5.2)–(5.4) with $Q=0$, such that (5.2) is simply

$$h_i=\int_{\Phi_b}^{\Phi_t}\frac{-\sigma'}{\mathcal{G}\phi}\,\mathrm{d}\phi, \tag{5.5}$$

with $\Phi_t=\sigma^{-1}(\mathcal{S}_0)$ and $\Phi_b=\sigma^{-1}(\mathcal{S}_0+\mathcal{G}\phi_0)$.

5.2. *Solutions*

Figure 11 illustrates the behaviour of flow-induced compaction for a pre-strained medium. If the applied pressure drop is less than the lift-off pressure, $|\mathcal{P}|\leqslant\mathcal{P}_{lift}$, then the entry pressure $\sigma(\Phi_e)$ is reduced but not relieved, the depth h is unchanged from h_i, and the profile of solid fraction ϕ rearranges, simultaneously compacting and decompacting in different regions. Alternatively, if $|\mathcal{P}|\geqslant\mathcal{P}_{lift}$, then the entry boundary is stress-free, h is

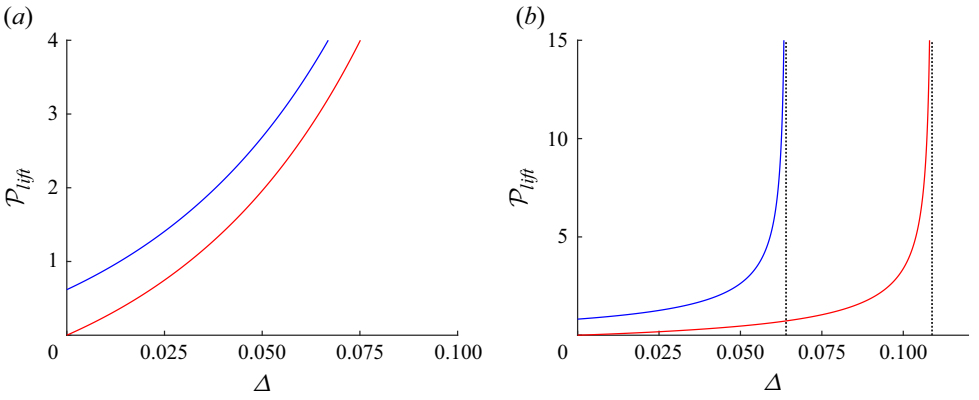

Figure 12. Lift-off pressure $\mathcal{P}_{lift}$ against the amount of pre-strain $\Delta = (h_g - h_i)/h_g$ for compaction induced by a downward flow (red) and upward flow (blue) with $\mathcal{G} = 0.5$. The media are governed by constitutive laws (2.19) with (*a*) $\lambda = 3$, a type 1 medium, and (*b*) $\lambda = 1$, a type 2 medium. Black dotted asymptotes in (*b*) correspond to $\Delta = (h_g - h_\infty)/h_g$, where h_∞ is the limiting compaction depth for an unpre-strained system.

reduced from h_i, and the medium can no longer decompact with ϕ strictly increasing. Figure 11(*a*) highlights the difference in lift-off pressure due to the orientation of flow: downward flow has a much lower lift-off pressure $\mathcal{P}_{lift}$. As before, upward flow admits the possibility of homogenising the medium as increasing applied pressure drop passes through $\mathcal{P} = \mathcal{G}\phi_0$ and the gradient of solid fraction changes sign (figure 11*d*).

Figure 11(*b*) compares the pre-strained evolution of h as $|\mathcal{P}|$ increases with the unpre-strained evolution of h, and illustrates how, once $\sigma(\Phi_e)$ is relieved, the pre-strained depth exactly coincides with the unpre-strained depth. The steady solutions of the pre-strained medium see no history of being mechanically compressed once $|\mathcal{P}| \geqslant \mathcal{P}_{lift}$. By corollary, we deduce that $\mathcal{P}_{lift}$ is exactly the applied pressure drop required to compact the unpre-strained medium to the pre-strain depth h_i. Similarly, Q in figure 11(*c*) is identical to the unpre-strained solution once $|\mathcal{P}| \geqslant \mathcal{P}_{lift}$, and as before, flux is higher in the upward flow than the downward flow.

In order to measure the relative strain from the no-flow state, we introduce the parameter $\Delta = (h_g - h_i)/h_g$, which quantifies the amount of pre-strain relative to the gravity-slumped depth h_g. Figure 12 presents the lift-off pressure $\mathcal{P}_{lift}$ for increasing Δ. The solutions contrast upward and downward flow, and type 1 and type 2 media. These graphs have some analogy with figure 8, which illustrated how increasing $\mathcal{G}$ directly increased $\mathcal{P}_{lift}$. Much like gravitational compaction, mechanical pre-strain increases the solid fraction throughout the medium towards the maximum solid fraction ϕ_m, increasing the effective pressure and decreasing the permeability; consequently, $\mathcal{P}_{lift}$ increases with Δ. We note that in both types of media in figure 12, $\mathcal{P}_{lift}$ is non-zero at zero strain Δ for upward flow corresponding to the gravitational lift-off pressure that is characteristic of upward flows.

The behaviour discussed thus far is independent of the 'type' of the medium. However, there is some difference between the two types as we increase Δ. Since $\mathcal{P}_{lift}$ is exactly the pressure required to compact an unpre-strained medium to the pre-strained depth h_i, there is no lift-off pressure in type 2 media if they are sufficiently pre-strained. More specifically, this occurs if the medium is mechanically compacted beyond the limiting flow-induced compaction depth h_∞. Since flow-induced compaction cannot induce sufficient force to reach depths $h_i \leqslant h_\infty$ in the unpre-strained regime, it also cannot relieve the associated pre-strain pressure exerted by mechanical compaction of the medium to this depth.

This feature is illustrated in figure 12(*b*) by the asymptotes for $\mathcal{P}_{lift}$ at values of the pre-strain coefficient $\Delta(h_i = h_\infty)$. In contrast, in a type 1 medium, $\mathcal{P}_{lift}$ exists for all attainable pre-strain depths $h_i > h_m$ (figure 12*a*).

6. Discussion

In this paper, we have extended two-phase modelling for the flow-induced compaction of soft porous media to consider its interaction with gravitational forces and compaction by an external load. We presented and interpreted theoretical solutions for a steady one-dimensional system in which a flow is induced either upwards or downwards across the medium, with the possibility of pre-straining. We considered general (nonlinearly) elastic media characterised by constitutive laws for permeability $k(\phi)$ and effective pressure $\sigma(\phi)$.

The behaviour of the medium in response to flow can be broadly categorised based on the relative interplay of the effective pressure and the permeability as the solid fraction approaches its limiting value; this, in turn, can be characterised by the poroelastic diffusivity function $D = k\phi\,\partial\sigma/\partial\phi$. In 'type 1' media (relatively more rigid: $(\phi_m - \phi)D \to \infty$ as $\phi \to \phi_m$), the flux increases without bound as the applied pressure drop is increased. In contrast, in 'type 2' media (relatively softer: $(\phi_m - \phi)D$ bounded as $\phi \to \phi_m$), flux increases up to an asymptotic value as the applied pressure drop increases, such that the medium becomes effectively insensitive to applied pressure changes; there are also corresponding asymptotic compaction depths and solid fraction profiles. Type 2 media may be further categorised into three subgroups based on their asymptotic solid fraction profiles.

The influence of gravitational compaction is characterised by the gravity term $\mathcal{G} = \Delta\rho\, g h_0/\sigma^*$, analogous to the ratio of the medium's depth to its natural compaction length scale $\sigma^*/\Delta\rho\, g$. Soft porous media naturally 'gravity-slump' and compact to a non-uniform profile of solid fraction that enforces a difference between upward and downward flow. While downward flow can only compact the medium, upward flow, for low applied pressure drop, simultaneously compacts and decompacts the medium, maintaining a fixed depth; the gravitational pressure on the lower boundary must first be relieved before bulk compaction occurs. We found that for sufficiently large $\mathcal{G}$, bulk compaction in upward flow cannot occur in type 2 media, as flow is unable to induce sufficient compaction to fully 'undo' gravitational compaction. For a given excess applied pressure drop, downward flow induces greater bulk compaction, reducing the bulk permeability and increasing the medium's resistivity to flow, thus resulting in a reduced flux compared to upward flow.

We further considered the case in which the medium is confined between porous plates at a depth less than its rest-state depth, which we refer to as 'pre-strained'. Pre-straining places the medium under a uniform pre-strain pressure, which can be reduced by flow-induced compaction and decompaction. Much like unpre-strained upward flow, the entry boundary pressure must be relieved for bulk compaction to occur. The applied pressure at which the depth begins to evolve, the lift-off pressure, is identically the applied pressure drop required to induce sufficient compaction on an equivalent unpre-strained medium to reach the pre-strained depth. Therefore, the lift-off pressure is dependent on the medium type, the amount of pre-strain compaction, the relative strength of gravity and the flow direction. These dependencies imply first, that the lift-off pressure is lower for downward flow than for upward flow, and second, that if a type 2 medium is pre-strained beyond its characteristic asymptotic depth, then no such lift-off pressure exists. Practically, we can use knowledge of the unpre-strained case to inform understanding of the pre-strained case, specifically to control if and when the pre-strain pressure is relieved.

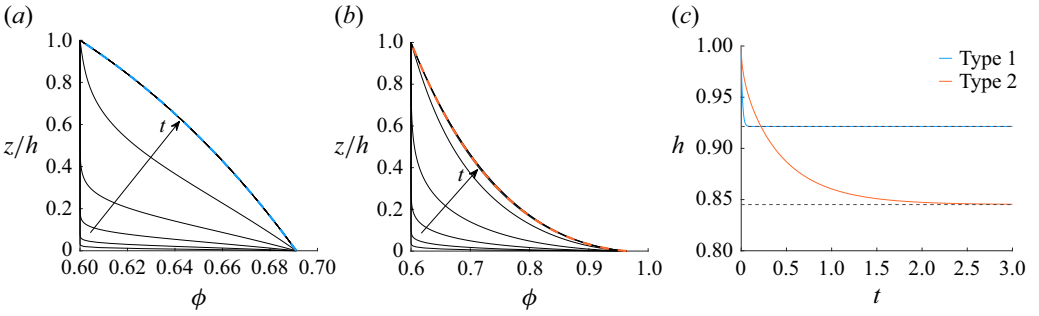

Figure 13. Transient solutions for (a,b) profiles of solid fraction ϕ and (c) the depth h for media compacted by a downward flow with a step increase from $\mathcal{P}=0$ at $t=0$ to $\mathcal{P}=-10$, evolving until $t=3$ with $\mathcal{G}=0$. The respective steady solutions are overlaid in dashed lines on each plot. The media are governed by effective pressure law (2.19) with (a) $\lambda=4$, a type 1 medium (blue lines), (b) $\lambda=1$, a type 2 medium (orange lines).

Although the effects of pre-strain and gravity-slumping are expected intuitively and observed industrially, the results outlined here are yet to be quantified experimentally. There is scope for simple experimental validation of the results. The most easily measured quantity might be the lift-off pressure, which we showed has significantly different values in upward and downward flow when there is notable gravity-slumping. For example, flow-induced compaction of hydrogel beads, a type 2 medium, is experimentally well established (MacMinn *et al.* 2015; Hewitt *et al.* 2016*a*) and would be a suitable candidate for comparing unpre-strained and pre-strained compaction to determine lift-off pressure.

Further considerations may include extending beyond the context of elastic media; open questions remain about how mechanical or gravitational compaction interact with flow-induced compaction of media governed by other constitutive laws. For example, how does the non-recoverable compaction of plastic media affect our understanding of gravity slumping or pre-straining? Beyond just the rheological behaviour of the medium, most geophysical, biological and industrial media are rather more complicated than the one-dimensional, homogeneous medium explored here. In particular, industrial products often contain defects that introduce significant spatial dependency of the reference stress-free solid fraction. It would be interesting to explore how flow-induced compaction interacts with inhomogeneities in two- and three-dimensional settings, especially in the development of preferential flow paths.

Funding. E.R.B. acknowledges the support of Saint-Gobain.

Declaration of interests. The authors report no conflict of interest.

Appendix A. Transient solutions

The transient model is governed by (2.1)–(2.4), which can be manipulated to form a nonlinear advection–diffusion equation for solid fraction and solved numerically with a second-order finite difference method and a semi-implicit adaptive time-stepping scheme.

Figure 13 presents the transient evolution of solid fraction ϕ and depth h, which each clearly reach their steady values. When a pressure drop is applied, the solid fraction at the boundary out of which fluid flows instantaneously adopts a higher solid fraction. The rest of the medium subsequently compacts, initially in a localised layer at the boundary, and gradually spreading across the depth of the medium until the steady solution is reached. Note that the evident difference in time scale for each medium to reach the steady state in figure 13 originates from the choice of constitutive laws. For the same applied $\mathcal{P}$, the

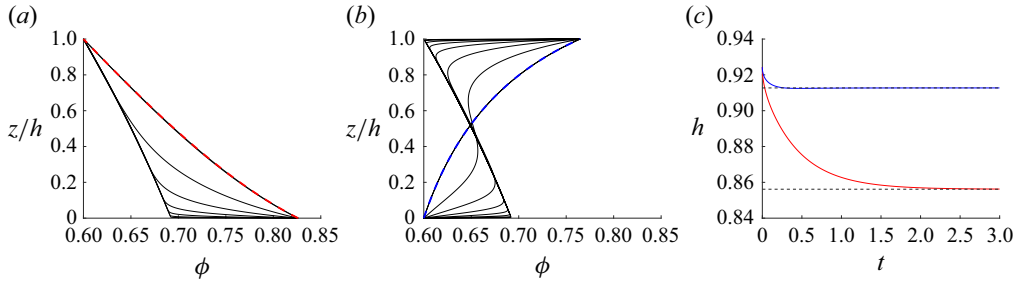

Figure 14. Transient solutions for (*a*,*b*) profiles of solid fraction ϕ and (*c*) the depth h for media compacted by flow (*a*) downwards (red lines) and (*b*) upwards (blue lines) induced by a step increase from $\mathcal{P}=0$ at $t=0$ to $|\mathcal{P}|=1$, evolving until $t=3$ with $\mathcal{G}=0.5$. The respective steady solutions are overlaid in dashed lines on each plot. The medium is governed by effective pressure law (2.19) with $\lambda=1$, a type 2 medium.

type 2 medium in figure 13(*c*) is compacted to a higher solid fraction, thus has a reduced permeability, increasing the time taken to squeeze fluid out and adjust towards the steady state.

We can similarly model the transient evolution of compaction with gravitational stresses ($\mathcal{G}>0$) and pre-strain $\mathcal{S}_0>0$. In this case, when a flow is instantaneously applied, the relieved pressure $\Sigma(\mathcal{P})$ is instantaneously reduced to the steady value as pressure is exerted on the solid matrix by the fluid. Figure 14 illustrates the compaction of a gravity-slumped medium (without pre-strain) with applied pressure drop $|\mathcal{P}|$ above the gravitational lift-off pressure. Much like in the $\mathcal{G}=0$ example in figure 13, changes in solid fraction are initially localised to the boundaries and subsequently spread across the depth of the medium, evolving towards the steady profiles (figure 14*a*,*b*). With upward flow, the lower boundary immediately becomes stress-free and the upper boundary compacts, such that we observe the simultaneous compaction and decompaction of the medium as gravitational compaction is 'undone'. We note that there is an immediate decrease and evolution of depth (figure 14*c*); lift-off is instantaneous when a pressure drop above the lift-off pressure is applied. The overall adjustment time scale is larger for downward flow, again because the solid fraction is pushed to higher values than in upward flow, which lowers the permeability and slows the evolution. The pre-strained transient solutions are qualitatively the same.

Appendix B. 'Types' of behaviour with $\mathcal{G}>0$

The separation of porous media into types based on constitutive laws was analysed in § 3.2 for $\mathcal{G}=0$. We present here the extension to $\mathcal{G}>0$.

Since $\mathcal{G}>0$, upward and downward flow analysis must be conducted independently. An expression for $\partial Q/\partial|\mathcal{P}|$ in downward flow is found from differentiation of (2.15) with respect to $|\mathcal{P}|$:

$$-\frac{k\sigma'\phi}{Q-k\mathcal{G}\phi}\bigg|_{\Phi_b}\frac{\partial\Phi_b}{\partial|\mathcal{P}|}-\int_{\Phi_b}^{\Phi_t}\frac{k\sigma'\phi}{(Q-k\mathcal{G}\phi)^2}\frac{\partial Q}{\partial|\mathcal{P}|}\,\mathrm{d}\phi=0, \tag{B1}$$

$$\Longrightarrow\frac{\partial Q}{\partial|\mathcal{P}|}=-\frac{\dfrac{k\phi}{Q-k\mathcal{G}\phi}\bigg|_{\Phi_b}}{\displaystyle\int_{\Phi_b}^{\Phi_t}\frac{k\sigma'\phi}{(Q-k\mathcal{G}\phi)^2}\,\mathrm{d}\phi}, \tag{B2}$$

with $\partial\Phi_b/\partial|\mathcal{P}| = 1/\sigma'(\Phi_b)$. We assume that $\sigma' > 0$ such that increasing the solid fraction increases the effective pressure. For downward flow, $Q < 0$ and $\Phi_b \geqslant \Phi_t$, so by simple inspection, $\partial Q/\partial|\mathcal{P}| < 0$ or equivalently $\partial|Q|/\partial|\mathcal{P}| > 0$.

For upward flow with $Q > 0$, the same differentiation of (2.15) is considered, and we reach an expression similar to (B2):

$$\frac{\partial Q}{\partial \mathcal{P}} = \frac{1}{\displaystyle\int_{\Phi_b}^{\Phi_t} \frac{k\sigma'\phi}{(Q - k\mathcal{G}\phi)^2}\,\mathrm{d}\phi} \left(\frac{\partial \Phi_t}{\partial \mathcal{P}} \frac{k\sigma'\phi}{Q - k\mathcal{G}\phi}\bigg|_{\Phi_t} - \frac{\partial \Phi_b}{\partial \mathcal{P}} \frac{k\sigma'\phi}{Q - k\mathcal{G}\phi}\bigg|_{\Phi_b} \right), \tag{B3}$$

where boundary conditions give

$$\Phi_t = \sigma^{-1}(\mathcal{P} - \Sigma(\mathcal{P})) \quad \Longrightarrow \quad \frac{\partial \Phi_t}{\partial \mathcal{P}} = \left(1 - \frac{\partial \Sigma}{\partial \mathcal{P}}\right) \frac{1}{\sigma'} > 0, \quad \text{since } \Sigma < \mathcal{P}, \tag{B4}$$

$$\Phi_b = \sigma^{-1}(\mathcal{G}\phi_0 - \Sigma(\mathcal{P})) \quad \Longrightarrow \quad \frac{\partial \Phi_t}{\partial \mathcal{P}} = -\frac{\partial \Sigma}{\partial \mathcal{P}} \frac{1}{\sigma'} < 0, \quad \text{since } \Sigma > 0, \tag{B5}$$

with inequalities following from bounds on the relieved pressure, which ensure that effective pressure is everywhere positive. The prefactor in (B3) is negative if $\Phi_t < \Phi_b$ (or equivalently, $\mathcal{P} < \mathcal{G}\phi_0$) and positive if $\Phi_t > \Phi_b$ (or $\mathcal{P} > \mathcal{G}\phi_0$). Since this directly corresponds to $Q \lessgtr k\mathcal{G}\phi$ for all $\phi \in [\Phi_b, \Phi_t]$, we can conclude that $\partial Q/\partial \mathcal{P} > 0$. Therefore, it holds true for all flows that Q may either increase without bound or increase up to an asymptotic limit as ϕ increases.

To consider the separation of porous media into two types with $\mathcal{G} > 0$, we cannot consider directly the integration of (B2)–(B3) as they are dependent on Q. Instead, we return to the implicit integral definition of Q in (2.15) in the limit $\mathcal{P} \to \infty$. The integral domain may be split into a region near to the compacted boundary solid fraction (e.g. Φ_b in downward flow) and the remaining domain. In the larger domain, there is an $O(1)$ contribution from the integrand, therefore the large-ϕ behaviour of Q is determined up to a constant by the compacted boundary domain. In this domain, $\phi \to \phi_m$, and as defined in (3.3), we can again substitute generic power law behaviour for permeability and effective stress. Since we have already determined that Q is either unbounded or tends to a constant, Q is dominant in the denominator as $\mathcal{G}(\phi_m - \phi)^\alpha \phi \to 0$; this contribution is effectively independent of gravity, therefore so is the separation into bounded or unbounded flux behaviour. As before, in (3.4)–(3.6), flux is unbounded as ϕ increases for $\alpha \leqslant \beta$, type 1 media, and flux increases to an asymptotic limit for $\alpha > \beta$, type 2 media.

The gradient of solid fraction $\partial\phi/\partial z$ at the compacted boundary is found from the definition of flux in (2.12). In the limit $\phi \to \phi_m$, this is expressed as

$$\frac{\partial \phi}{\partial z} \approx -\frac{1}{\beta} Q(\phi_m - \phi)^{1+\beta-\alpha} + \frac{1}{\beta} \mathcal{G}\phi(\phi_m - \phi)^{\beta+1} \quad \text{as } \phi \to \phi_m, \tag{B6}$$

which differs from the $\mathcal{G} = 0$ analysis by the addition of the second gravity-dependent term. This additional term disappears as $\phi \to \phi_m$, so the separation of type 2 media into types 2*i*, 2*ii*, 2*iii* based on the limit of the gradient is the same as in the $\mathcal{G} = 0$ case.

References

Audet, D.M. & Fowler, A.C. 1992 A mathematical model for compaction in sedimentary basins. *Geophys. J. Intl* **110** (3), 577–590.

Bear, J. 1996 Modeling transport phenomena in porous media. In *Environmental Studies* (ed. M.F. Wheeler), pp. 27–63, Springer.

Biot, M.A. 1941 General theory of three-dimensional consolidation. *J. Appl. Phys.* **12** (2), 155–164.

BOROVINŠEK, M., TAHERISHARGH, M., VESENJAK, M., REN, Z. & FIEDLER, T. 2016 Geometrical characterization of perlite-metal syntactic foam. *Mater. Charact.* **119**, 209–215.
BOSCHETTI, F., PENNATI, G., GERVASO, F., PERETTI, G.M. & DUBINI, G. 2004 Biomechanical properties of human articular cartilage under compressive loads. *Biorheology: Official J. Intl Soc. Biorheol.* **41** (3–4), 159–166.
BUSCALL, R. & WHITE, L.R. 1987 The consolidation of concentrated suspensions. Part 1. The theory of sedimentation. *J. Chem. Soc. Faraday. Trans. 1: Phys. Chem. Condens. Phase* **83** (3), 873–891.
CARMAN, P.C. 1997 Fluid flow through granular beds. *Chem. Engng Res. Des.* **75**, S32–S48.
CAMERON, N.M. & RAPP, C.F. 2001 Fiberglass. In *Encyclopedia of Materials: Science and Technology*, pp. 3142–3146. Elsevier.
CHU, C.P. & LEE, D.J. 2002 Dewatering of waste activated sludge via centrifugal field. *Dry. Technol.* **20** (4–5), 953–966.
CHU, C.P., LEE, D.J. & TAY, J.H. 2003 Gravitational sedimentation of flocculated waste activated sludge. *Water Res.* **37** (1), 155–163.
CONCHA, F. & BÜRGER, R. 2002 A century of research in sedimentation and thickening. *KONA Powder Particle J.* **20** (0), 38–70.
COUSSY, O. 2004 *Poromechanics*. John Wiley & Sons.
FENG, J.J. & YOUNG, Y.-N. 2020 Boundary conditions at a gel–fluid interface. *Phys. Rev. Fluids* **5** (12), 124304.
FIEDLER, T., MOVAHEDI, N., YORK, L. & BROXTERMANN, S. 2020 Functionally-graded metallic syntactic foams produced via particle pre-compaction. *Metals* **10** (3), 314.
FIORI, M., PRAMANIK, S. & MACMINN, C.W. 2023 Flow and deformation due to periodic loading in a soft porous material. *J. Fluid Mech.* **974**, A2.
FIORI, M., PRAMANIK, S. & MACMINN, C.W. 2025 Solute transport due to periodic loading in a soft porous material. *J. Fluid Mech.* **1009**, A15.
FITT, A.D., HOWELL, P.D., KING, J.R., PLEASE, C.P. & SCHWENDEMAN, D.W. 2002 Multiphase flow in a roll press nip. *Eur. J. Appl. Maths* **13** (3), 225–259.
FUNG, Y.C. 2013 *Biomechanics: Mechanical Properties of Living Tissues*. Springer Science & Business.
HEAD, J.W. & WILSON, L. 1992 Magma reservoirs and neutral buoyancy zones on Venus: implications for the formation and evolution of volcanic landforms. *J. Geophys. Res.: Planets* **97** (E3), 3877–3903.
HEWITT, D.R., CHINI, G.P. & NEUFELD, J.A. 2018 The influence of a poroelastic till on rapid subglacial flooding and cavity formation. *J. Fluid Mech.* **855**, 1170–1207.
HEWITT, D.R., NIJJER, J.S., WORSTER, M.G. & NEUFELD, J.A. 2016*a* Flow-induced compaction of a deformable porous medium. *Phys. Rev. E* **93** (2), 023116.
HEWITT, D.R., PATERSON, D.T., BALMFORTH, N.J. & MARTINEZ, D.M. 2016*b* Dewatering of fibre suspensions by pressure filtration. *Phys. Fluids* **28** (6), 063304.
KHALED, A.R.A. & VAFAI, K. 2003 The role of porous media in modeling flow and heat transfer in biological tissues. *Intl J. Heat Mass Transfer* **46** (26), 4989–5003.
DE KRETSER, R.G., BOGER, D.V. & SCALES, P.J. 2003 Compressive rheology: an overview. In *Rheology Reviews*, pp. 125–165. British Society of Rheology.
LANDMAN, K.A., SIRAKOFF, C. & WHITE, L.R. 1991 Dewatering of flocculated suspensions by pressure filtration. *Phys. Fluids A: Fluid Dyn.* **3** (6), 1495–1509.
LANDMAN, K.A. & WHITE, L.R. 1994 Solid/liquid separation of flocculated suspensions. *Adv. Colloid Interface Sci.* **51**, 175–246.
MACMINN, C.W., DUFRESNE, E.R. & WETTLAUFER, J.S. 2015 Fluid-driven deformation of a soft granular material. *Phys. Rev. X* **5** (1), 011020.
MACMINN, C.W., DUFRESNE, E.R. & WETTLAUFER, J.S. 2016 Large deformations of a soft porous material. *Phys. Rev. Appl.* **5** (4), 044020.
MANGA, M. & BRODSKY, E. 2006 Seismic triggering of eruptions in the far field: volcanoes and geysers. *Annu. Rev. Earth Planet. Sci.* **34**, 263–291.
MERGNY, C. & SCHMIDT, F. 2024 Gravity-induced ice compaction and subsurface porosity on icy moons. *Icarus* **413**, 116008.
S.-D.E-LA MUELA, A.M., CAMBRONERO, L.E.G. & RUIZ-ROMÁN, J.M. 2020 Molten metal infiltration methods to process metal matrix syntactic foams. *Metals* **10** (1), 149.
PARKER, K.H., MEHTA, R.V. & CARO, C.G. 1987 Steady flow in porous, elastically deformable materials. *J. Appl. Mech.* **54** (4), 794–800.
PATERSON, D.T., EAVES, T.S., HEWITT, D.R., BALMFORTH, N.J. & MARTINEZ, D.M. 2019 Flow-driven compaction of a fibrous porous medium. *Phys. Rev. Fluids* **4** (7), 074306.

PATERSON, D.T., EAVES, T.S., HEWITT, D.R., BALMFORTH, N.J. & MARTINEZ, D.M. 2021 On two-phase modeling of dewatering pulp suspensions. *AIChE J.* **67** (9), e17277.

RICHES, P.E., DHILLON, N., LOTZ, J., WOODS, A.W. & MCNALLY, D.S. 2002 The internal mechanics of the intervertebral disc under cyclic loading. *J. Biomech.* **35** (9), 1263–1271.

SMIT, T.H. 2022 Finite element models of osteocytes and their load-induced activation. *Curr. Osteoporosis Rep.* **20** (2), 127–140.

SMITH, J.E. 1971 The dynamics of shale compaction and evolution of pore–fluid pressures. *J. Intl Assoc. Math. Geol.* **3** (3), 239–263.

STICKLAND, A.D. & BUSCALL, R. 2009 Whither compressional rheology? *J. Non-Newtonian Fluid Mech.* **157** (3), 151–157.

TERZAGHI, K. 1943 *Theoretical Soil Mechanics*. John Wiley and Sons, Inc.

VAN ZESSEN, E., TRAMPER, J., RINZEMA, A. & BEEFTINK, H.H. 2005 Fluidized-bed and packed-bed characteristics of gel beads. *Chem. Engng J.* **115** (1–2), 103–111.

WAKEMAN, R.J. 2007 Separation technologies for sludge dewatering. *J. Hazard. Mater.* **144** (3), 614–619.

WILSON, L. & HEAD, J.W. 1994 Mars: review and analysis of volcanic eruption theory and relationships to observed landforms. *Rev. Geophys.* **32** (3), 221–263.

WORSTER, M.G., PEPPIN, S.S.L. & WETTLAUFER, J.S. 2021 Colloidal mushy layers. *J. Fluid Mech.* **914**, A28.

XU, Z., YUE, P. & FENG, J.J. 2024 *Estimating the interfacial permeability for flow into a poroelastic medium*. *Soft Matt.* **20** (37), 7357–7361.

XU, Z., ZHANG, J., YOUNG, Y.-N., YUE, P. & FENG, J.J. 2022 Comparison of four boundary conditions for the fluid–hydrogel interface. *Phys. Rev. Fluids* **7** (9), 093301.